THE MORPHOLOGICAL DEMOGRAPHICS OF GALAXIES IN THE ACS HUBBLE ULTRA DEEP PARALLEL FIELDS[†]

FELIPE MENANTEAU[1], HOLLAND C. FORD[1], VERÓNICA MOTTA[2,1], NARCISO BENÍTEZ[3,1]
ANDRÉ R. MARTEL[1], JOHN P. BLAKESLEE[1] AND LEOPOLDO INFANTE[2]
Accepted for publication in the Astronomical Journal

ABSTRACT

We present a morphological analysis of distant field galaxies using the deep ACS images from the public parallel NICMOS observations of the Hubble Ultra Deep Field obtained in the F435W (B_{435}), F606W (V_{606}), F775W (i_{775}) and F850LP (z_{850}) filters. We morphologically segregate galaxies using a combination of visual classification and objective machine based selection. We use the Asymmetry (A) and Central Concentration (C) parameters to characterize galaxies up to $z_{850,AB} < 25$ mag. We take advantage of the multicolor dataset and estimate redshifts for our sample using the Bayesian photometric redshift (BPZ) which enables us to investigate the evolution of their morphological demographics with redshift. Using a template fitting model and a maximum likelihood approach, we compute the star-formation rate (SFR) for galaxies up to $z \simeq 1.3$ and its contributions from different morphological types. We report that spirals are the main providers to the total SFR. The E/S0s contribution flattens out at $z \simeq 1$ while the Irr/Pec populations continuously rise to match the spirals contribution at $z \simeq 1.0$. We use the $i_{775} - z_{850}$ and $V_{606} - i_{775}$ color-magnitude diagrams to constrain the galaxies' formation histories and find that E/S0s show both a population of luminous red galaxies in place at $z \sim 1.2$ and a bluer and fainter population resembling those of Irr/Pec at similar redshifts.

Subject headings: galaxies: evolution — galaxies:structure — galaxies:formation — galaxies: elliptical and lenticular, cD

1. INTRODUCTION

The archeological nature of galaxy evolution studies prevents us from following individual galaxies over time. In consequence we are only left with snapshots at different lookback times from where we attempt, as excavators, to piece together their evolutionary histories from the motion of different observable quantities and their inter-relationships through different cosmic times. As morphology correlates with a range of physical properties in galaxies, such as mass, luminosities and particularly color, this suggest that their appearance must embody some important clues about their formation histories. Moreover, the growing acceptance of the notion that the morphological appearance of galaxies may not be a static property set at an early stage of formation, makes it crucial to understand the flow of the morphological mix of galaxies and their observables as a function of redshifts.

The early morphological studies of HST galaxies (Cowie et al. 1995; van den Bergh et al. 1996; Volonteri et al. 2000; Reshetnikov et al. 2003) set the stage for the Advanced Camera for Surveys (ACS; Ford et al. 2002) to effortlessly resolve galaxies at ever fainter limits thus enabling the study of the morphological demographics of distant galaxies with larger and deeper datasets (see Elmegreen et al. 2004a,b, 2005, for a list of recent studies). Since its installation, ACS has provided a continuous flow of high resolution optical imaging of distant field galaxies over significantly wider areas. Large programs such as GOODS (Giavalisco et al. 2004b), GEMS (Rix et al. 2004) and the ACS/GTO (Postman et al. 2005; Ford et al. 2002) have spawned several studies that address the color evo-

lution of galaxies, the number evolution of red objects with redshift (Bell et al. 2004), the mass assembly rate for different morphologies (Bundy et al. 2005) and constrain the ages and masses of early types (Treu et al. 2005; Menanteau et al. 2004).

In this paper we take advantage of public deep multicolor ACS parallel observations to study the morphological color and star formation rate evolution of galaxies at depths comparable to those of the Hubble Deep Fields (Williams et al. 1996), but probing areas many times larger. Throughout this paper we use $H_0 = 70$ km s^{-1}Mpc^{-1} and a flat ($\Omega_k = 0$) cosmology with $\Omega_M = 0.3$ and $\Omega_\Lambda = 0.7$. Magnitudes are given in the AB system across the paper.

2. OBSERVATIONS

2.1. *ACS Multicolor Imaging*

Our analysis is based on the deep ACS parallel fields of the Near Infrared Camera and Multi-Object Spectrometer (NICMOS) imaging of the Hubble Ultra Deep Field (UDF) (GO 9803, PI: Thompson). The ACS datasets consist of two separate fields around the center of the UDF arranged in a mosaiced pattern determined by the NICMOS observations of $30''$ spacing between pointings (Blakeslee et al. 2004). The resulting coverage of the parallel ACS fields as well as the UDF and NICMOS observations positions are shown in Fig 1. Each field comprises 9, 9, 18, and 27 orbits in the F435W (B_{435}), F606W (V_{606}), F775W (i_{775}) and F850LP (z_{850}) filters respectively. The images are publicly available from the STScI archive and were processed using the ACS/GTO pipeline (Apsis; Blakeslee et al. 2003a) which includes object detection, photometry and cataloging using SExtractor (Bertin & Arnouts 1996). Photometry was calibrated in AB magnitudes using the zeropoints from Sirianni et al. (2005). Photometric redshifts were also computed using the Bayesian estimator BPZ from Benítez (2000). Within the deepest regions of the fields the 10σ limited magnitudes were 28.8, 29.0, 28.5 and 27.8 in B_{435}, V_{606}, i_{775} and z_{850} respectively

[1] Department of Physics and Astronomy, Johns Hopkins University, 3400 North Charles Street, Baltimore, MD 21218.
[2] Departmento de Astronomía y Astrofísica, Pontificia Universidad Católica de Chile, Casilla 306, Santiago 22, Chile.
[3] Instituto de Astrofísica de Andalucía (CSIC), Camino Bajo de Huétor 24, Granada 18008, Spain
[†] Based on observations obtained with the Hubble Space Telescope and at Las Campanas Observatory.
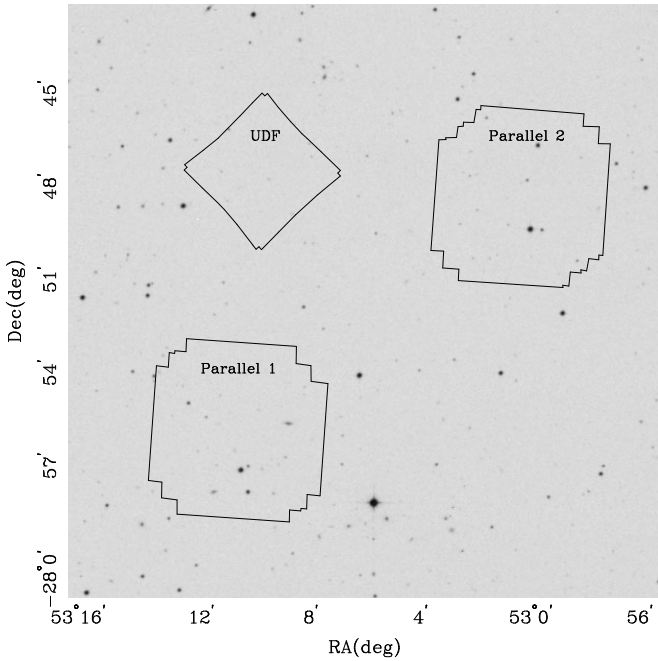
FIG. 1.— The diagram of the relative positions and sizes of the final mosaiced patterns of the ACS parallel observations of the UDF NICMOS and the ACS/UDF observations.

(Bouwens et al. 2004) in a scale of $0.''05$ pixel^{-1}. The final ACS area covered was 55.7 arcmin^2 from both fields. For a detailed description of the dataset and its processing we refer to Blakeslee et al. (2004).

2.2. *LDDS2 Magellan Spectra*

Follow up multi-object spectroscopy on one of the parallel fields was performed using the low-dispersion survey spectrograph 2 (LDSS2) on Las Campanas Observatory Magellan Clay 6.5m Telescope. A complete description of the observations and data reduction analysis of the spectroscopic sample is given in Motta et al. (2005); here we briefly summarize these observations. For Field #1 three masks were observed in November 25 and 26, 2003 from which spectra for a total of 56 galaxies were secured. From these we secured redshifts for 51, and for a subset of 37 galaxies line strengths and equivalent widths (EW) were measured. Targets for the masks were uniformly selected from galaxies within the field with $i_{775} < 23$. The spectra were reduced using a combination of a customized IDL reduction software techniques optimized for the extraction of background limited data (Frye et al. 2002) and IRAF tasks for the wavelength and flux calibrations. The final integrated exposure times per mask were between 7200s and 4800s at a central wavelength of 5500Å and spectral coverage of $4000 - 9000$Å at 5.3Å pixel^{-1} dispersion.

2.3. *Morphological Classification*

Rather than using the color of galaxies as a surrogate for morphological type, in this paper we exploit the superb ability of ACS to resolve and morphologically segregate distant galaxies with no a priori built-in biases in the selection criteria. We classified galaxies according to their morphologies down to $z_{850,AB} < 25$ using a two-pronged approach based on visual inspections and automated classifications. First, galaxies were visually inspected and classified using the Medium Deep Survey (MDS) scheme as described in Abraham et al.

(1996b) and modified by Menanteau et al. (1999) (see also Treu et al. 2005). Within this system we segregated galaxies into three broad categories: *i)* E/S0 which include E, E/S0 and S0; *ii)* Spirals: including Sa+b, S and Sc+d and *iii)* Irr/Pec including Irregular and Peculiar types. We also limited our sample to objects with $> 90\%$ confidence in their BPZ redshift estimates. We elaborate on this in the next section. A final catalog containing 1228 galaxies was visually inspected by one of us (FM) in both ACS fields.

Secondly, we independently investigated the morphologies of galaxies using automated classifications. For this we calculated the central concentration (C) and asymmetry (A) parameters for all galaxies using the definitions from Abraham et al. (1994, 1996b). Our analysis is based on the well-known relationship between the A and C structural parameters and traditional visual morphologies (Abraham et al. 1996a,b; Brinchmann et al. 1998; Conselice 2003) We compute asymmetry and concentration using PyCA , our own automated Python software. The code is designed to compute A and C from the SExtractor products generated by Apsis, the detection catalog and associated segmentation image. However, it can be used with any standard SExtractor products and it is publicly available[5].

Concentration is computed as the ratio between the flux at 30% of a given radius $0.3R$ to the total flux up to that radius R. Formally it is defined as,

$$C = f(0.3R)/f(R), \quad (1)$$

were $f(R) = 2\pi \int_0^R I(r)dr$ is the integrated flux within the radius R. The determination of the radius R up to where to integrate the light is of importance particularly for the asymmetry values. As we sample galaxies over ever larger cosmic ages, the surface brightness of galaxies at higher redshifts become heavily affected by the well-known $(1 + z)^4$ cosmological dimming (Tolman 1934; Sandage & Lubin 2001). Therefore to consistently measure structural parameters of galaxies over similar physical areas at different redshifts, we chose an aperture radius defined as $R_p = 1.5 \times r_p$, with $\eta = 0.2$, where r_p is the Petrosian (1976) radius and $\eta(r) = I(r)/\langle I(r) \rangle$ is the ratio of the galaxy average surface brightness, $I(r)$, in an annulus of radius r and the mean value up to the same radius, $\langle I(r) \rangle$ (see Papovich et al. 2003; Blanton et al. 2001; Menanteau et al. 2004, and references therein). The advantage of using a Petrosian radius over traditional surface brightness limits ones, such as the Holmberg radius (i.e. Abraham et al. 1996a; Menanteau et al. 1999) is that it only depends on the galaxy light profile and it is therefore independent of the redshift of observation (see Bershady et al. 2000, for a discussion). Comparatively accurate results can be obtained using the SExtractor Kron radius, which in most cases coincides with R_p.

Similarly, asymmetry is computed as half of the ratio between the absolute value of subtraction of the image, I_{ij}, and its 180° rotated image around its center, I_{ij}^R, to the original image, both contained in an elliptical mask of semi-major length R_p. To avoid variations arising from noise features, the pivot point of the galaxies was computed after the images were smoothed with a Gaussian kernel of 1 pixel and then self-subtracted. Formally, our working definition for asymmetry

---

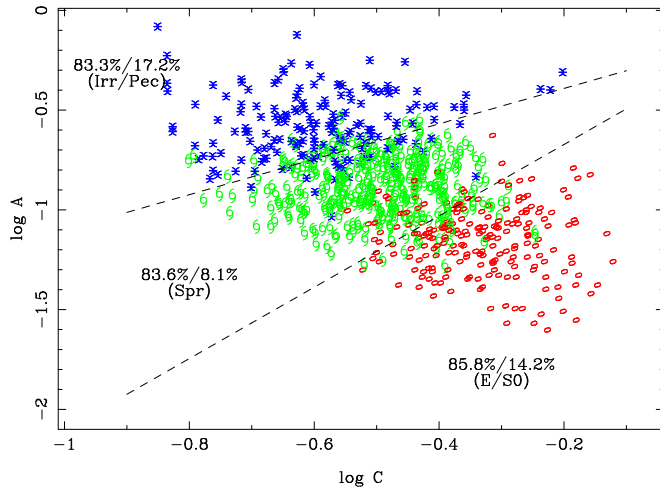[5] It can be downloaded from http://acs.pha.jhu.edu/~felipe/PyCA

FIG. 2.— The asymmetries and central concentrations values keyed to their visual morphological classes for all 768 objects in the Field #1. E/S0 systems are represented by ellipses; Spiral galaxies by spirals and Irr/Pec as asterisks. The dashed lines represent the selection limits based on $A - C$ that maximizes the recovery of visual classes and minimizes the contamination from other morphological types. Numbers inside the figure represent the recovery and contamination percentages of visual classes and from other classes respectively using the A and C based selection.

over a galaxy with an intensity matrix I_{ij} can be expressed as,

$$A = \frac{1}{2} \frac{\sum |I_{ij} - I_{ij}^R| - b}{\sum I_{ij}}. \quad (2)$$

Because we use the absolute values of the self-subtracted galaxy residuals, small variations in the image background can appear even in the most symmetric objects, consequently we add a factor b to correct for this artificial A signal introduced, such as $b = \sqrt{2}\sigma_{sky}N_{pix}$, where N_{pix} is the area inside the ellipse mask and σ_{sky} is the sky mean standard deviation.

We compute A and C for all objects in our galaxy sample to a limiting magnitude $z_{850,AB} < 25$. To avoid morphological variations resulting from redshifting bandpass (i.e. morphological $K-$correction), we compute A and C using the image in the closest available band to the rest-frame B derived from the photometric redshift information. In Fig. 2 we show the distribution of asymmetry and concentration for galaxies in Field #1 as function of their visual morphological classes. We only show structural values for one field to avoid overcrowding in the diagram. Results are similar for Field #2. This type of diagram has been extensively used to illustrate and calibrate the morphological segregation of galaxies based purely on machine classifications (see Abraham et al. 1996a,b; Menanteau et al. 1999). We use this approach to isolate galaxies in the same three equivalent broad visual morphological categories. The A–C classification recovers $\gtrsim 80\%$ of the visual classifications in all three categories, with contaminations of $\lesssim 15\%$ from other classes. We will use this criteria to isolate galaxies based on $A - C$ and compare their properties in the next section.

3. ANALYSIS

One of the objectives in this paper is to investigate the cosmic star formation history and its dependence on morphological type. To accomplish this we need to obtain reliable SFRs for a large number of galaxies. Because of the faint limits of the sample and the large number of objects involved,
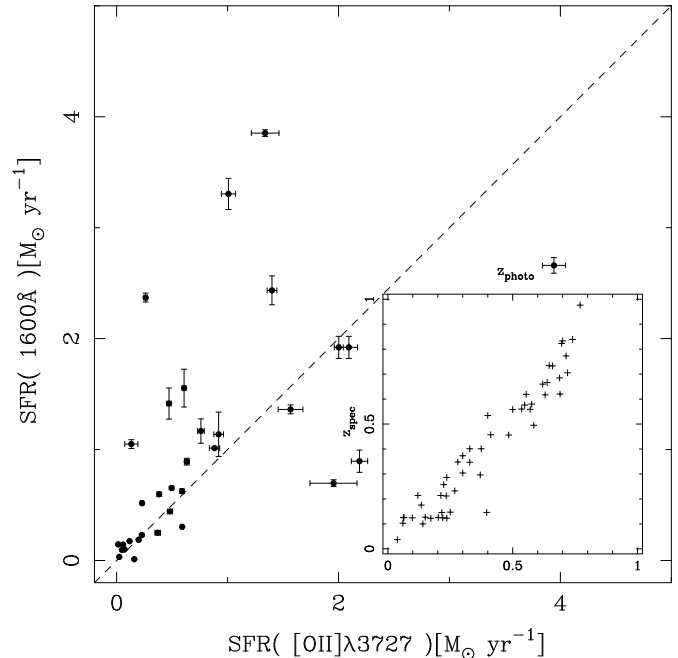

FIG. 3.— The star formation rate (SFR) from the spectroscopic sample of galaxies derived from the [O II]λ3727 EW compared to the SFR estimation based on the 1600Å UV flux. The inset panel shows the relation between the BPZ photometric redshifts estimates and the spectroscopic ones from our ground-based observations.

securing spectroscopic diagnostic for all of them would be extremely time consuming, and in most cases unfeasible because of their faintness. Instead, we chose to follow an approach that takes advantage of the deep and precise ACS multicolor photometric information, and we use ancillary ground-based spectroscopy and UV imaging for a control sample of galaxies to validate our results.

3.1. The UV SFR at 1600Å

There are several SFR indicators based on transformation between ultraviolet flux and star formation activity (see Steidel et al. 1999; Coe et al. 2005; Hopkins et al. 2001, 2004, for a discussion and references therein). We opt for computing the SFR for each galaxy using the prescription of Meurer et al. (1999). This is straightforward and computationally easy to implement, and derived from a constant SFR and a Salpeter initial mass function with limits $0.1 - 100\ M_\odot$. They define the ultraviolet flux at 1600Å, F_{1600}, as the integrated light over a square synthetic filter of width 350Å and central rest-frame wavelength at 1600Å. Based on this, Meurer et al. (1999) provide a direct transformation between a galaxy's SFR and F_{1600} such as

$$\text{SFR}[M_\odot \text{yr}^{-1}] = 10^{-0.4(M_{1600}+18.15)}$$

and M_{1600} is the F_{1600} corresponding absolute magnitude in AB system.

Because our ACS filter information only spans between $\sim 3500 - 9000$Å, the galaxies' rest-frame UV light only falls into our bluest band for $z > 1.5$. However, due to the large number of objects involved in this study and their precise photometry it is possible to derive a general description the galaxies' spectral energy distribution (SED). We utilize the galaxy's reconstructed SED from their BPZ spectral type, T_B, and based on this we estimated the galaxy's UV light

at 1600Å and compute their rest-frame F_{1600} flux. The T_B–types provided by BPZ are a linear combination from a template library of SEDs. We use the CWWSB_Benitez2003 template set as described in Benítez et al. (2004). These are based on the templates from Coleman, Wu, & Weedman (1980) and Kinney et al. (1996) consisting of El, Sbc, Scd, Im, SB3, and SB2, which represent the typical SEDs of elliptical, early/intermediate type spiral, late-type spiral, irregular, and two types of starburst galaxies respectively. This template set has been modified from earlier BPZ versions to remove differences between the predicted colors and those of real galaxies, which results in improved BPZ estimates (see Benítez et al. 2004, for details). We note that Coe et al. (2005) have followed a similar approach to estimate the UV-SFR using also the template fits from BPZ for $z < 6$ galaxies in the HUDF, but at 1400Å instead.

However, because new stars are born in dusty regions, their observed UV light can be strongly attenuated and our observed UV SFRs are therefore subject to obscuration. In order to account for this we must correct the SFR estimates for dust extinction. We use the empirical relationship between the unobscured far-infrared (FIR) flux and the intrinsic SFR (SFR$_i$) prescription by Hopkins et al. (2001), as FIR light penetrates the dust and provides reliable SFR$_i$. The Hopkins et al. empirical formulation between the (obscured) observed-UV SFR, SFR$_o$, at a given wavelength λ and their SFR$_i$ is,

$$\log(\mathrm{SFR}_i) = \log(\mathrm{SFR}_o) - 0.346 \times k(\lambda)$$
$$\times \log\left[\frac{0.797\log(\mathrm{SFR}_i) + 3.834}{2.88}\right], \quad (3)$$

where SFRs are in units of $[\mathrm{M}_\odot \mathrm{yr}^{-1}]$ and $k(\lambda)$ is the empirical Calzetti et al. (2000) attenuation law, $k(\lambda) = A(\lambda)/E(B-V)$ This improper equation must be solved numerically to obtain the extinction-corrected SFR$_i$ for a given observed UV SFR$_o$. We compute the corrected SFR for our full sample for $\lambda = 1600$Å using $k(1600) = 9.97$. This same method has also been used in the HUDF for high redshift galaxies (see Coe et al. 2005 and references therein). In the next section we use the corrected SFR$_i$ to calculate the star formation density evolution as a function of morphological type.

3.2. *Emission Line vs. Synthetic SFR*

We compare our SFR estimates obtained using the 1600Å flux with independent SFR measurement from traditional EWs. For this, we utilize the EW from the [O II]λ3727 emission lines to estimate SFR using the prescription from Kennicutt (1998) using the control-sample of galaxies from our LDDS2 spectroscopic campaign. In Fig 3 we show the individual SFR$_{1600}$ estimates from our synthetic approach and the ones obtained from [O II]λ3727 EWs. For the majority of galaxies there is good agreement between the two measurements, showing a clear relation between both estimators. We find that although there are minor discrepancies for individual galaxies, the overall agreement between SFR$_{1600}$ and [O II]λ3727 is quite satisfactory and we estimate out typical uncertainties to be ΔSFR/SFR ~ 0.3. As in this paper we target the general properties for the population as a whole rather than the precise characterization of each galaxy, we are confident that our template-based SFR yield meaningful results.

3.3. *Comparing Synthetic UV fluxes with GALEX observations*
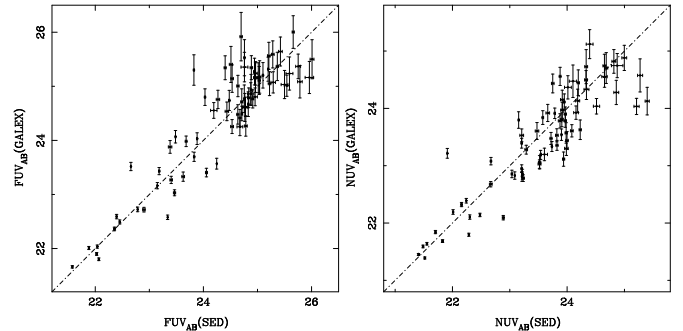

FIG. 4.— The GALEX observed FUV (left panel) and NUV (right panel) magnitudes compared to the synthetic recovered values using the reconstructed spectral energy distributions from the BPZ template library set. GALEX FUV and NUV error bars come from the original errors in the GALEX catalogs. Synthetic error bars reflect only original ACS photometric errors.

We further investigate our ability to model the galaxies' UV light by comparing our synthetic estimates of the UV flux with the observed magnitudes obtained from overlapping Galaxy Evolution Explorer (GALEX, Martin et al. 2005) observations for the same ACS regions. We retrieved the positions, FUV(1530Å) and NUV (2310Å) magnitudes and associated errors in the AB system from the MAST/GALEX Web Archive[6] and matched them with the galaxies in our ACS sample. From a total of 165 GALEX sources in both fields, we successfully identified 71 galaxies in our sample with both FUV and NUV magnitudes. We compute the synthetic magnitudes through the FUV and NUV bandpasses for each of the matched galaxies using the reconstructed SEDs. In Figure 4, we show the comparison of real and synthetic values of FUV and NUV. We find that the real and modeled values agree well, with a nominal mean scatter $\Delta(UV_{\mathrm{GALEX}} - UV_{\mathrm{SED}})$ of 0.31 and 0.36 mags for FUV and NUV respectively. Therefore, we conclude that our UV flux estimates for ACS galaxies represent a good description of their real values and can be used as surrogates when measuring the SFR for large samples of galaxies.

4. MORPHOLOGICAL DEMOGRAPHICS BETWEEN $0.3 < Z < 1.2$

4.1. *The morphological SFR density*

There is a plethora of studies that have focused on the evolution of the SFR density, $\rho_{\mathrm{SFR}}(z)$, at intermediate redshifts (Gallego et al. 1995; Madau et al. 1996; Lilly et al. 1996; Flores et al. 1999; Glazebrook et al. 2004) and high redshifts (Giavalisco et al. 2004a; Bouwens et al. 2004; Coe et al. 2005). These studies have found that SFR rises rapidly from $z = 0$ to $z = 1$ and peaks somewhere at $z > 2 - 3$ depending on the role of obscuration and our ability to unearth missing galaxies at higher redshifts. However, there is little information about how the global SF history is distributed into galaxy types (e.g. according to morphology). Only a few attempts have been made to address this issue using relatively small, but deep, sample such as the Hubble Deep Fields (see Brinchmann et al. 1998; Menanteau et al. 2001). In this paper we aim to separate the contributions to the global SFR from each of the morphological classes up to $z \simeq 1$. Many studies have addressed the evolution of $\rho_{\mathrm{SFR}}(z)$ in detail and at high redshifts, but a full census of the contribution from individual morphological classes is yet missing.
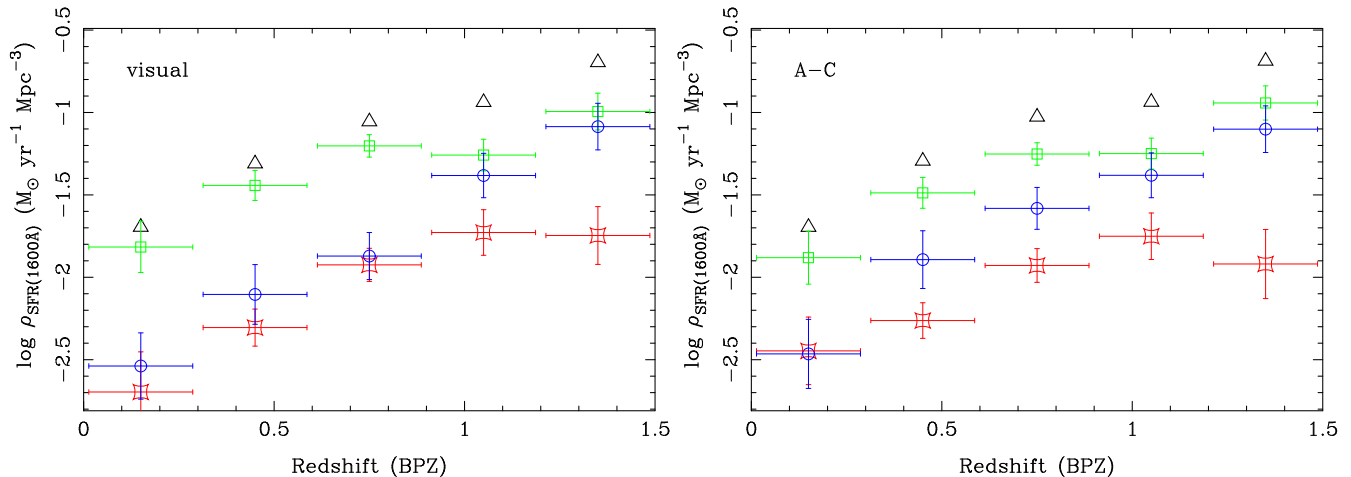
[6] http://galex.stsci.edu/GR1

FIG. 5.— The co-moving star formation density of galaxies as a function of redshift for the three morphological groups. Red rounded squares represent E/S0s, green squares, Spirals and blue circles Irr/Pec selected galaxies. Bars represent 1σ deviations. Open triangles represent the total star formation density from all classes. The left panel shows the results from morphologically selecting galaxies according to their visual classes, while the right panel shows the results from the A–C automatic selection.

We calculate the SFR density for each morphological class at given redshift interval $z_1 < z < z_2$ as,

$$\rho_{\mathrm{SFR}}(z) = \sum_{j, z_1 < z_j < z_2} \frac{\mathrm{SFR}_j}{V_{max,j}} \qquad (4)$$

where we sum the star formation contribution of each galaxy, SFR_j, for $z_1 < z_j < z_2$ and V_{max} is the co-moving volume at z_{max}, the highest redshift at which a given galaxy, j, is still brighter than our sample limiting magnitude, $z_{850,\mathrm{AB}} < 25$ (Schmidt 1968). We proceed in this fashion for all galaxies, and calculate $\rho_{\mathrm{SFR}}(z)$ for the E/S0, Spirals and Irregular/Peculiar samples. We explore the morphological selection calculating $\rho_{\mathrm{SFR}}(z)$ using both the visual morphological classifications and the machine-based selection. In Fig. 5 we show the results of $\rho_{\mathrm{SFR}}(z)$ for the visual and automatic classifications. We also show the total $\rho_{\mathrm{SFR}}(z)$ as well as the contribution of the three subclasses. We note that E/S0s are, as expected, the lowest contributors to the total $\rho_{\mathrm{SFR}}(z)$ regardless of the classification used. We see from the figure that there are only small differences in $\rho_{\mathrm{SFR}}(z)$ from the two approaches, mostly in the selection of E/S0 and Irr/Pec. Moreover, the star formation density for early-types shows a modest increase with redshift which seems to flatten out by $z \simeq 1$. This is not the case of either of the other classes or the global $\rho_{\mathrm{SFR}}(z)$. On the other hand the Irr/Pec galaxies show a constant and in step increase with redshift virtually matching the contribution from Spirals, the most active group, by $z \simeq 1$.

4.2. Differential Evolution

We investigate the morphological evolution of galaxies using the observed color magnitude diagrams at several redshift intervals. Our motivation arises from the recognition that early-types in clusters exhibit a tight correlation between their colors and magnitudes. This correspondence, known as the color-magnitude relation (CMR) or "red sequence", has been widely used to constrain the ages of galaxies, particularly for cluster ellipticals (see Bower et al. 1992; Blakeslee et al. 2003b, and references). and in recent years also for field galaxies at different cosmic times (Bell et al. 2004, Kodama, Bower, & Bell 1999). Galaxies at similar evolutionary stages should have comparable colors, while departures from this

can be employed to establish variations in their star formation history and be interpreted as differential evolution within their stellar population, regardless of its origin (i.e secular evolution or recent mergers).

We construct the color magnitude (CM) diagrams for $i_{775} - z_{850}$ and $V_{606} - i_{775}$ colors as a function of z_{850} at three evenly spaced redshift intervals, $0.3 < z < 0.6$, $0.6 < z < 0.9$ and $0.9 < z < 1.2$. We chose to avoid the $z < 0.3$ objects because they are highly incomplete and undersampled. Each interval's diagram is a snapshot of the galaxies' current evolutionary phase, where dispersions in their color can be interpreted as variations (or lack of) in their age and star formation history. Despite the relative large width of our redshift bins, we can use them to provide a general census of the galaxies' relative formation stages as a function of their morphology.

In Fig 6 we plot the diagrams keyed to their visual morphological type, for $V_{606} - i_{775}$ in the left panel and $i_{775} - z_{850}$ on the right one. We use the same symbols as in Fig. 2. When focusing on the red envelope of galaxies, we see that this is dominated by morphologically selected E/S0 galaxies in all redshift bins. Although there is considerable scatter, a red sequence of passively evolved E/S0 is quite distinguishable. We also show the $z = 0.023$ Coma Cluster CMR (Bower et al. 1992) transformed to the intervals' central redshift and transformed from $U - V$ to $i_{775} - z_{850}(z)$ and $V_{606} - i_{775}(z)$ accordingly. We use empirical and synthetic templates (Bruzual & Charlot 2003; Coleman, Wu, & Weedman 1980) to transform between $\Delta(U - V)$ to $\Delta(i_{775} - z_{850})$ and $\Delta(V_{606} - i_{775})$ respectively. The redshifted Coma CMR represents a bonafide benchmark for old and coeval early-type systems. For the highest redshift $i_{775} - z_{850}$ interval we plot the empirical CMR for the $z = 1.237$ CL1252-2927 cluster as derived by Blakeslee et al. (2003b). In each of the panels we also show with a solid star the redshifted values of $M_B^\star$ from the COMBO17 survey (Wolf et al. 2003) to z_{850} at the central redshift of each interval. This insures that even in our highest redshift bin we are probing galaxies at ~ 2 magnitudes deeper than $M^\star$ within the flux limit of our sample.

Previous CMR studies of HST morphologically selected field galaxies show similar results. The Kodama, Bower, & Bell (1999) analysis of ellipticals in the Hubble Deep Field
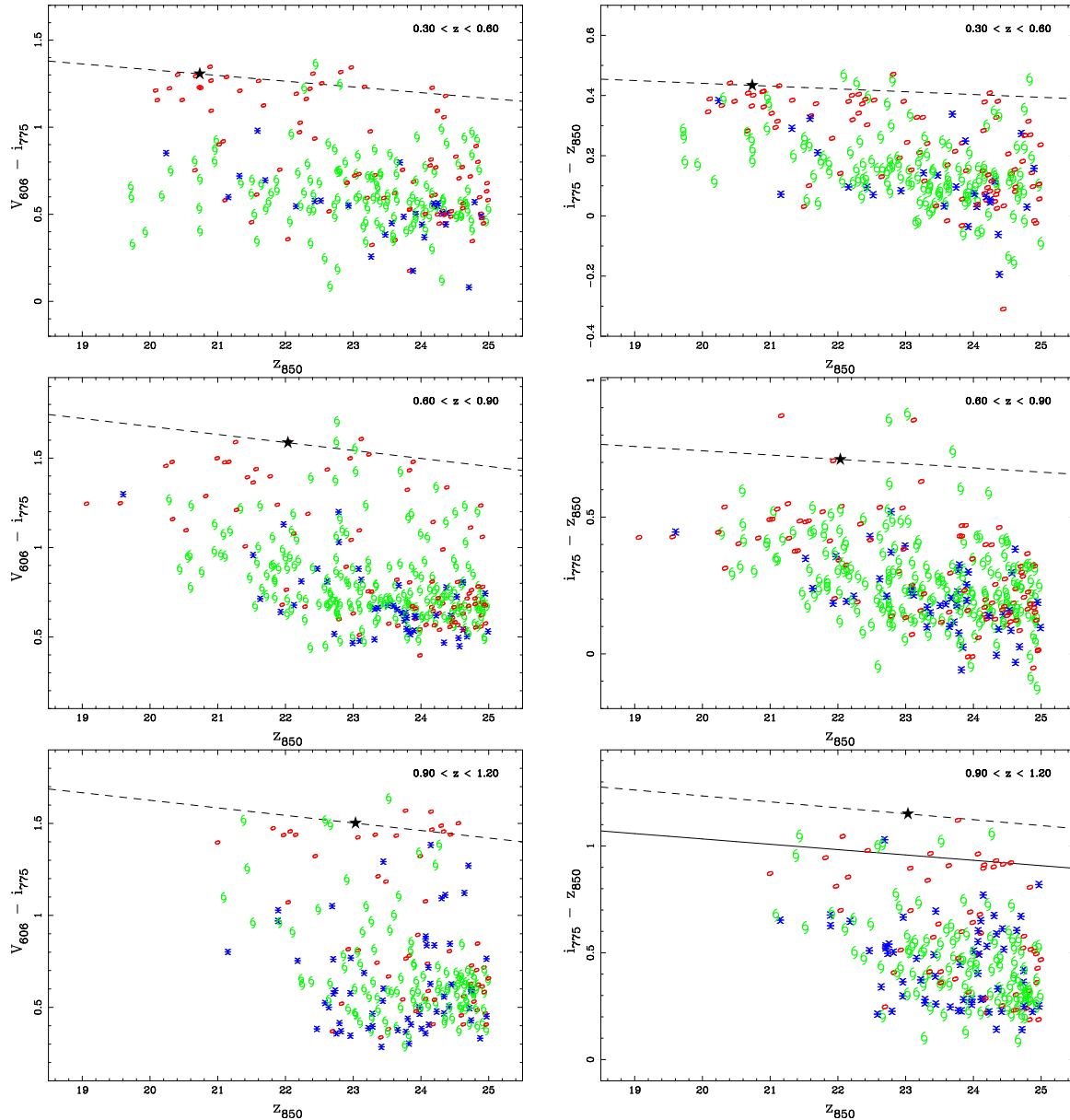
FIG. 6.— The $V_{606} - i_{775}$ and $i_{775} - z_{850}$ observed color magnitude diagrams as a function of $z_{850,AB}$ magnitude for three evenly spaced redshift intervals between $z = 0.3 - 1.2$. Symbols are the same as in Fig. 2 and are keyed to their visual morphological classes. E/S0 systems are represented by ellipses; Spiral galaxies by spirals and Irr/Pec as asterisks. The dashed lines represent the color magnitude relation for E/S0s for the Coma Cluster redshifted to mean interval redshift of each panel. The solid line in the right panel is the empirical relation for CL1252-2927 at $z = 1.237$ from Blakeslee et al. (2003b). For comparison we show as solid stars the values of $M_B^\star$ from the COMBO17 survey (Wolf et al. 2003) for early types redshifted to z_{850} at the mean redshift of each interval.

North at $\langle z \rangle \sim 0.9$ was the first to report the presence of a red sequence of field ellipticals at that redshift, comprising around $\sim 1/2$ of the population of early types. However, a significant fraction have bluer rest-frame colors, which Menanteau et al. (2001) later reported to be also coincidental with having large internal color dispersions. In a later larger sample, Bell et al. (2004) using GEMS observations confirmed the presence of a red sequence dominated by early types $(70\% - 80\%)$ at $z \sim 0.7$. These studies establish a pattern in morphologically selected samples of spheroids where systems are predominantly old and coeval, but bluer and presumably younger ellipticals coexist at intermediate redshifts (see Menanteau et al. 1999; Kodama et al. 1999; Abraham et al. 1999; Menanteau et al. 2001, 2004; Benson et al. 2002; Cross et al. 2004).

In this paper we report a similar behavior. We note that while E/S0s tend to dominate the red envelope, there is an important fraction of systems with significantly bluer colors than those of old ellipticals. Moreover, redder E/S0s tend to be brighter (massive) than bluer ones, which are systematically fainter at all redshifts. This result favors a view in which most massive ellipticals might have formed at higher redshift and where at least an important fraction of those were already in place at $z \simeq 1$. However, it is unclear whether bluer early-type galaxies will become the present day massive systems we see in place. We note that it is unlikely that these bluer systems could be confused with the brightest knots of faint irregular galaxies, as it has been established that ACS can efficiently distinguish between such contrasting galaxy types at these limits, and especially in these high signal-to-noise images (see Cross et al. 2004; Conselice et al. 2004; Menan-

teau et al. 2004). Spiral galaxies display a broad range of colors, and nearly uniform distribution of magnitudes over all redshift ranges with observed magnitudes similar to those of the brightest E/S0s in the red envelope. Irregular and Peculiar galaxies, on the other hand, tend to dominate the low luminosity loci with predominantly bluer colors, but comparable to the blue E/S0 systems. While these two groups — blue E/S0 and Irregular/Peculiars— have dramatically different structural properties, their similarities in colors and luminosities make it tantalizing to relate the evolutionary histories of these two very different types.

5. SUMMARY

In this paper we have investigated the properties of a large morphologically selected sample of ACS galaxies. The deep multicolor information and ancillary ground-based spectroscopy has enabled us to constrain the evolution of the SFR density and the individual contribution to the global $\rho_{\rm SFR}(z)$. We report that spiral galaxies are the main providers to the global SFR density at all redshifts, while the E/S0s' humble contribution starts to flatten out by $z = 1$. We note that Irregular and Peculiar galaxies show the sharpest and continuous rise with redshifts, reaching similar levels as spirals at $z \simeq 1.2$. We use the observed color magnitude diagram to constrain the relative ages and formation histories of galaxies for different morphologies. We report that E/S0s are the predominant population of red and luminous galaxies at all redshift. We confirm, however, the presence of a population of much bluer and fainter early-type galaxies, with colors and luminosities resembling those of the irregular and peculiar galaxies. Upcoming deep far-ultraviolet observations of the Ultra Deep Field will gives a clearer view of the star-forming nature of galaxies in the UV window.

REFERENCES

Abraham, R. G., Ellis, R. S., Fabian, A. C., Tanvir, N. R., & Glazebrook, K. 1999, MNRAS, 303, 641

Abraham, R. G., Tanvir, N. R., Santiago, B. X., Ellis, R. S., Glazebrook, K., & van den Bergh, S. 1996a, MNRAS, 279, L47

Abraham, R. G., Valdes, F., Yee, H. K. C., & van den Bergh, S. 1994, ApJ, 432, 75

Abraham, R. G., van den Bergh, S., Glazebrook, K., Ellis, R. S., Santiago, B. X., Surma, P., & Griffiths, R. E. 1996b, ApJS, 107, 1

Bell, E. F. et al. 2004, ApJ, 600, L11

Benítez, N. 2000, ApJ, 536, 571

Benítez, N. et al. 2004, ApJS, 150, 1

Benson, A. J., Ellis, R. S., & Menanteau, F. 2002, MNRAS, 336, 564

Bershady, M. A., Jangren, A., & Conselice, C. J. 2000, AJ, 119, 2645

Bertin, E., & Arnouts, S. 1996, A&AS, 117, 393

Blakeslee, J. P., Anderson, K. R., Meurer, G. R., Benítez, N., & Magee, D. 2003a, in Astronomical Data Analysis Software and Systems XII ASP Conference Series, Vol. 295, 2003 H. E. Payne, R. I. Jedrzejewski, and R. N. Hook, eds., p.257, 257–+

Blakeslee, J. P. et al. 2003b, ApJ, 596, L143

—. 2004, ApJ, 602, L9

Blanton, M. R. et al. 2001, AJ, 121, 2358

Bouwens, R. J. et al. 2004, ApJ, 606, L25

Bower, R. G., Lucey, J. R., & Ellis, R. S. 1992, MNRAS, 254, 601+

Brinchmann, J. et al. 1998, ApJ, 499, 112

Bruzual, G., & Charlot, S. 2003, MNRAS, 344, 1000

Bundy, K., Ellis, R. S., & Conselice, C. J. 2005, ApJ, 625, 621

Calzetti, D., Armus, L., Bohlin, R. C., Kinney, A. L., Koornneef, J., & Storchi-Bergmann, T. 2000, ApJ, 533, 682

Coe, D., Benitez, N., Ford, H., & et al. 2005, ApJ submitted

Coleman, G. D., Wu, C.-C., & Weedman, D. W. 1980, ApJS, 43, 393

Conselice, C. J. 2003, ApJS, 147, 1

Conselice, C. J. et al. 2004, ApJ, 600, L139

Cowie, L. L., Hu, E. M., & Songaila, A. 1995, AJ, 110, 1576

Cross, N. J. G. et al. 2004, AJ, 128, 1990

Elmegreen, D. M., Elmegreen, B. G., & Hirst, A. C. 2004a, ApJ, 604, L21

Elmegreen, D. M., Elmegreen, B. G., Rubin, D. S., & Schaffer, M. A. 2005, ApJ, 631, 85

Elmegreen, D. M., Elmegreen, B. G., & Sheets, C. M. 2004b, ApJ, 603, 74

Flores, H. et al. 1999, ApJ, 517, 148

Ford, H. et al. 2002, in Proc. SPIE Vol. 4854, p. 81-94, in Future EUV and UV Visible Space Astrophysics Missions and Instrumentation, J. C. Blades; O.H. Siegmund; Eds., 81–94

Frye, B., Broadhurst, T., & Benítez, N. 2002, ApJ, 568, 558

Gallego, J., Zamorano, J., Aragon-Salamanca, A., & Rego, M. 1995, ApJ, 455, L1+

Giavalisco, M. et al. 2004a, ApJ, 600, L103

—. 2004b, ApJ, 600, L93

Glazebrook, K., Tober, J., Thomson, S., Bland-Hawthorn, J., & Abraham, R. 2004, AJ, 128, 2652

Hopkins, A. M., Connolly, A. J., Haarsma, D. B., & Cram, L. E. 2001, AJ, 122, 288

Hopkins, P. F. et al. 2004, AJ, 128, 1112

Kennicutt, R. C. 1998, ARA&A, 36, 189

Kinney, A. L., Calzetti, D., Bohlin, R. C., McQuade, K., Storchi-Bergmann, T., & Schmitt, H. R. 1996, ApJ, 467, 38

Kodama, T., Bower, R. G., & Bell, E. F. 1999, MNRAS, 306, 561

Lilly, S. J., Le Fevre, O., Hammer, F., & Crampton, D. 1996, ApJ, 460, L1+

Madau, P., Ferguson, H. C., Dickinson, M. E., Giavalisco, M., Steidel, C. C., & Fruchter, A. 1996, MNRAS, 283, 1388

Martin, D. C. et al. 2005, ApJ, 619, L1

Menanteau, F., Abraham, R. G., & Ellis, R. S. 2001, MNRAS, 322, 1

Menanteau, F., Ellis, R. S., Abraham, R. G., Barger, A. J., & Cowie, L. L. 1999, MNRAS, 309, 208

Menanteau, F. et al. 2004, ApJ, 612, 202

Meurer, G. R., Heckman, T. M., & Calzetti, D. 1999, ApJ, 521, 64

Motta, V., Menanteau, F., Infante, L., & The ACS Team. 2005, AJ

Papovich, C., Giavalisco, M., Dickinson, M., Conselice, C. J., & Ferguson, H. C. 2003, ApJ, 598, 827

Petrosian, V. 1976, ApJ, 209, L1

Postman, M. et al. 2005, ApJ, 623, 721

Reshetnikov, V. P., Dettmar, R.-J., & Combes, F. 2003, A&A, 399, 879

Rix, H. et al. 2004, ApJS, 152, 163

Sandage, A., & Lubin, L. M. 2001, AJ, 121, 2271

Schmidt, M. 1968, ApJ, 151, 393

Steidel, C. C., Adelberger, K. L., Giavalisco, M., Dickinson, M., & Pettini, M. 1999, ApJ, 519, 1

Tolman, R. C. 1934, Relativity, Thermodynamics, and Cosmology (Relativity, Thermodynamics, and Cosmology, Oxford: Clarendon Press, 1934)

Treu, T. et al. 2005, ArXiv Astrophysics e-prints

van den Bergh, S., Abraham, R. G., Ellis, R. S., Tanvir, N. R., Santiago, B. X., & Glazebrook, K. G. 1996, AJ, 112, 359

Volonteri, M., Saracco, P., & Chincarini, G. 2000, A&AS, 145, 111

Williams, R. E. et al. 1996, AJ, 112, 1335

Wolf, C., Meisenheimer, K., Rix, H.-W., Borch, A., Dye, S., & Kleinheinrich, M. 2003, A&A, 401, 73